Performance analysis of a K2CO3-based thermochemical energy storage system using a honeycomb structured heat exchanger

Karunesh Kant, A. Shukla, David M J Smeulders, C.C.M. C M Rindt

Version of Record: https://www.sciencedirect.com/science/article/pii/S2352152X2100308X
Manuscript_c3fd641ae6c3ca963ec575951d258253

Performance analysis of a K_2CO_3-based thermochemical energy storage system using a honeycomb structured heat exchanger

Karunesh Kant[a*], A. Shukla[b], David M. J. Smeulders[a], C.C.M. Rindt[a]

[a]Department of Mechanical Engineering, Eindhoven University of Technology, 5600 MB-Eindhoven, Netherlands

[b]Non-Conventional Energy Laboratory, Rajiv Gandhi Institute of Petroleum Technology Jais, Amethi, UP 229304, India

[*]k1091kant@gmail.com,

Graphical Abstract

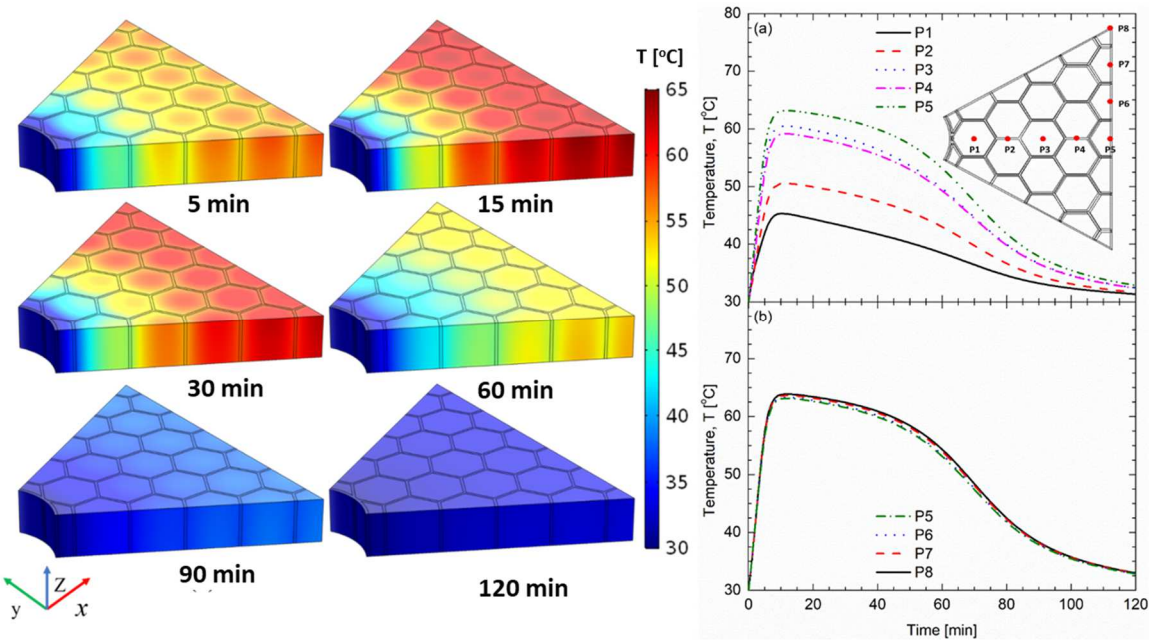

ABSTRACT

The application of thermal energy storage using thermochemical heat storage materials is a promising approach to enhance solar energy utilization in the built environment. Potassium carbonate (K_2CO_3) is one of the potential candidate materials to efficiently store thermal energy due to its high heat storage capacity and cost-effectiveness. In the present study, a 3-dimensional numerical model is developed for the exothermic hydration reaction of K_2CO_3. The heat produced from the reaction is transferred indirectly from the TCM bed through the

walls of the honeycomb heat exchanger to a Heat Transfer Fluid (HTF). A parametric study is conducted for varying geometrical parameters of the honeycomb heat exchanger. The obtained results indicate that the reaction rate and heat transport in the TCM bed strongly depends on the geometrical parameters of the heat exchanger. Reducing the cell size of the honeycomb heat exchanger up to a certain level provides better thermal transport as well as improved reaction rate of the TCM bed. The results of this study provide detailed insight into the heat release processes occurring in a fixed bed of K_2CO_3. The study is useful for designing and optimizing thermo-chemical energy storage modules for the built environment.

Keywords: Thermochemical; Hydration; Thermal Energy, Reaction; Energy Storage.

Nomenclature

C	*concentration [mol]*
C_p	*heat capacity [J/kgK]*
D_g	*water vapor diffusion coefficient* $[m^2/s]$
d_p	*particle diameter [m]*
k	*thermal conductivity [W/mK]*
L_C	*honeycomb cell length [m]*
M_v	*molar mass of water vapor [kg/mol]*
p	*pressure [Pa]*
p_{eq}	*equilibrium pressure [Pa]*
R	*ideal gas constant* $[J/mol\ K]$
$t_{gap,HTF}$	*distance between two HTF tubes [m]*
T	*temperature* $[^oC]$

u	*Darcy velocity [m/s]*
ε_{eff}	*effective bed porosity*
δ_{fin}	*honeycomb fin thickness [m]*
δ_b	*bed height [m]*
χ	*stoichiometric coefficient*
ρ	*density [kg/m^3]*

1. INTRODUCTION

Buildings are responsible for approximately 40% of the total energy consumption and for 36% of the total CO_2 emissions in the EU, ranking them at the top in terms of energy requirements. [1]. As stated by the European Commission [2], about 75% of the heating and cooling demand is still generated using fossil fuels while only 19% is generated from renewable energy sources. To achieve the EU's climate and energy goals, the heating and cooling sector must sharply reduce its energy consumption and also decrease the usage of fossil fuels. Fossil fuels are not only depleting but are also responsible for global climate change because of their induced rise in greenhouse gas emissions. Therefore, there is an urgent need to focus on renewable energy sources for the heating purposes of buildings. The application of renewable energy sources in the built environment is highly affected by the mismatch between the demand for energy and the supply of energy by renewable resources like solar energy and wind energy. The seasonal mismatch, particularly in the case of energy demand for heating applications, can be resolved up to a large extent by utilizing seasonal heat storage. The main idea is to store thermal energy in summer (high supply, low demand) and utilize it in winter (high demand, low supply). This can be achieved by developing technologies that can efficiently store thermal energy for a longer period with minimal losses. The basic mechanism for developing such technology lies in the property of certain materials that release heat when they ad/absorb water. This mechanism can be utilized to store heat from the sun by using solar heat to dry the material after water is absorbed. The energy stored can be released later by simply adding water vapor to the material.

The thermochemical energy storage (TCES) materials as introduced above are promising materials to store thermal energy utilizing a reversible chemical reaction [3–9]. In this reaction, a thermochemical energy storage material (C) absorbs external heat (e.g. solar energy, industrial waste heat) through an endothermic reaction, decomposing into A and B. Products (A and B) are separated by physical means and stored in separate containers. When materials A and B are combined again, an exothermic reverse reaction, generation of C, and release of stored thermal energy occur [10–14]. Although much work has been done in the direction of material characterization, identification, and improvement, as well as process integration and application, little effort has been put into closed thermochemical reactor modelling and process design [15–17]. Funayama et al. [7] suggested the thermal decomposition of calcium hydroxide ($Ca(OH)_2$) into calcium oxide (CaO) and water vapor as

a reversible gas-solid reaction suitable for TCES. The study focused on the development of composite honeycomb support composed of silicon carbide and silicon to enhance the heat transfer in a reaction bed. The results suggest that the heat transfer through the reaction bed was enhanced by the Si-SiC honeycomb support. Zhou et al. [18] developed a numerical model for TCES involving the energy balance and reaction kinetics describing the redox reaction of cobalt oxides (Co_3O_4/CoO pair), to simulate the phenomena of thermochemical storage. Metallic redox pair oxides such as BaO_2/BaO, Mn_2O_3/Mn_3O_4, CuO/Cu_2O and Fe_2O_3/Fe_3O_4 have been studied for CSP plants [19,20]. Ranjha and Oztekin [21] performed a numerical analysis of a three-dimensional bed with $Ca(OH)_2/CaO$ as the reaction pair. The results of the study provide detailed insight into the heat release processes occurring in a fixed bed of $Ca(OH)_2/CaO$ reaction pair. The study helps designing and optimizing high temperature thermo-chemical energy storage modules for power generation applications. One of the most promising chemical reaction systems for energy storage is the reaction utilising potassium carbonate and water vapor [22]:

$$\mathrm{K_2CO_3(s) + 1.5H_2O(g) \rightleftharpoons K_2CO_3 \cdot 1.5H_2O(s) + 1.5\Delta H_r}$$

Gaeini et al. [22] summed up the advantages of a $\mathrm{K_2CO_3 - K_2CO_3 \cdot 1.5H_2O}$ system with a storage capacity up to 96.015 kJ/mol (reaction enthalpy of ΔH_r,= 64.01kJ/mol of water) corresponding to a maximum energy density of 1.30 GJ/m^3 [23,24]. It features high material energy density and the reaction shows good reversibility. The drawbacks are that thermochemical energy storage materials, in general, have low thermal conductivity. The dehydration and hydration kinetics of the reactions involved are relatively well-identified.

This literature assessment indicates that numerical analysis, as well as experimental investigations of the TCES reactive materials and reactor design, has attracted considerable interest during the past few decades. Although sensible and latent heat storage systems have made their way into commercial applications, TCES (currently at the laboratory stage, mainly due to technical challenges) could be applied in many applications [20,25,26]. Therefore, numerical simulation tools to model the thermochemical reactions, understand the reaction kinetics, and optimize the system performance, are very essential. In the recent past, bionics based tools have been realized to be one of the advanced tools, especially in the field of fluid flow and heat transfer applications including chemical reactors [27], biomedical equipment [28,29], and electronic cooling [30–34]. The fin structures made by natural assortment

encourage the improvement of the TCES device. By realizing natural structures, the fins with bionic structures, for instance, tree-shaped fins [34,35], Koch fractal fins [36], and snowflake-shaped fins [37,38], have been proposed by researchers for their enhanced heat transport, subsequently increasing the thermal transport effectiveness of TCES devices. With the existence of honeycomb meshed structures in nature, the idea surfaced to solve the problem of thermal transport in a TCES device with the use of such a structure as a reactor bed. Therefore, the present work focuses on the performance analysis of TCES based on potassium carbonate (K_2CO_3) filled in a honeycomb heat exchanger structure.

The performance analysis has been achieved by studying heat and mass transfer through the reactive bed of $K_2CO_3 \cdot 1.5H_2O$ designed for a thermochemical heat storage system. The numerical model developed for the purpose has been solved using COMSOL Multiphysics software [39]. The study is performed to see the impact of the honeycomb heat exchanger on the recovery of the thermo-chemically-stored energy as well as the reaction rate in the TCM bed. Further, a parametric study has been conducted to investigate the effect of various honeycomb heat exchanger design parameters (i.e. honeycomb cell size $[L_c]$, honeycomb fin thickness $[\delta_{fin}]$, bed height $[\delta_b]$ and distance (denoted with subscript *gap*) in between two HTF tube $[t_{gap,HTF}]$) on the temperature variation, the reaction advancement and the recovery of the thermo-chemically-stored energy. These parameters are highly related to the heat exchanger design of the honeycomb structure. It is explicitly noted here that the material properties of potassium carbonate are considered to be constant during the reaction and that resulting effects like swelling/shrinking are not taken into account.

The work performed as presented in this article is organized in the following manner. Firstly, in the introduction section, the general background and the aim of this work are presented. After the introduction, the numerical model as developed in the present work is discussed including the mathematical formulation of the heat and mass transport equations employed in the TCM bed, the computational procedure, and the model validation. Further, the results of the numerical simulations and a parametric study for the hydration of the TCM bed are analyzed. Finally, a summary along with the key conclusions of the present work is presented in the last section.

2. GEOMETRY AND MODEL IMPLEMENTATION

The working pair of the material considered in the present study is potassium carbonate and water vapor. Olives and Mauran [40] showed that heat transfer in TCM bed through thermal radiation can be ignored as the working temperature of the thermochemical heat storage system considered here is in the range of 10 °C to 90 °C only. They further showed that, for a system with water vapor, the prevailing heat transfer mode is conduction. Heat transfer by convection in the porous medium can also be neglected as the reaction between the potassium carbonate and the water vapor is supposed to be instantaneous and gets completed so fast that there is no temperature difference between the salt and the water vapor and single temperature equations can be used for the macroscopic description of the heat transfer processes in the porous medium. The vapor transport in the TCM can be of Knudsen, Darcy, or inertial flow type since it depends on vapor pressure and velocity at the porous media boundaries. The fluid is considered to flow through the TCM bed consisting of approximately spherical particles with global porosity. Water vapor is considered an ideal gas, due to its low concentration and partial pressure. A relatively low permeability value of the porous bed (Table 1) makes it possible to model mass transfer with Darcy's law. The sensible heat of the reactive bed is also taken into account in the energy balance considering the sensible heat of water vapor and the stored heat in the salt as one entity. We also assume that the thermal conductivity and heat capacity of the salt are constants. The thermo-physical properties of potassium carbonate, water vapor, and operating parameters that have been used in the model are given in Table 1. The following assumptions have been made in the present study: (i) the properties of the phases are isotropic and uniform. Unless specified otherwise the physical and chemical properties of the constituents are assumed to be constant; (ii) the water vapor is in thermal equilibrium with the solid phase; (iii) The porous medium is not deformable; (iv) The gaseous adsorbate adheres to the ideal gas law; (v) The effects of pressure work and viscous dissipation are negligible.

Table 1. The thermophysical properties of TCM and operating parameters considered in the present study [22,41]

Name	Value	Description
d_p	$0.5 \times 10^{-3} m$	particle diameter
ε_{eff}	0.4	effective bed porosity
D_v	$10^{-9}\ m^2/s$	water vapor diffusion coefficient
$C_{p,v}$	$1864\ J/kgK$	heat capacity of water vapor

$C_{p,s}$	830 $J/kg\ K$	heat capacity of solid potassium carbonate
$C_{p,fin}$	900 $J/kg\ K$	heat capacity of fin material
ρ_s	2210 kg/m^3	the density of potassium carbonate
ρ_{fin}	2700 kg/m^3	density of fin
k_{eff}	0.44 $W/m\ K$	thermal conductivity of potassium carbonate
k_{fin}	238 $W/m\ K$	thermal conductivity of fin
E_a	46.22 kJ/mol	activation energy
M_v	0.01802 kg/mol	the molar mass of water vapor
M_s	0.138 kg/mol	the molar mass of K_2CO_3
χ	1.5	stoichiometric coefficient
ΔH_r	64.01 kJ/mol	reaction enthalpy kJ/mol of water
R	8.314 $J/mol\ K$	ideal gas constant
A_f	$3.0838 \times 10^6\ 1/min$	pre-exponential factor in reaction kinetics
T_i	30^oC	initial temperature
T_{eva}	15^oC	evaporator temperature
T_{HTF}	30^oC	cooling temperature of HTF
p_i	425 Pa	initial pressure
C_i	0.07 mol/m^3	initial concentration

The schematic of the honeycomb heat exchanger thermochemical reactor bed considered in the present study is illustrated in Fig. 1A. The system consists of several honeycomb heat exchanger beds filled with K_2CO_3 particles and separated at a distance to allow water vapor to reach the TCM material. The thickness of each honeycomb heat exchanger bed is indicated with δ_b. The heat transfer fluid (HTF) tubes are connected in the center to each heat exchanger unit in the system. The whole system is enclosed in a chamber where water vapor is injected from the evaporator and relatively cold water is flowing in the HTF tubes. An expanded side view of one honeycomb heat exchanger is presented in Fig. 1B, where hexagonal cells are connected to HTF tubes and the distance between two HTF tubes is given by $t_{gap,HTF}$. Further, the HTF tubes are arranged in such a way that they make a hexagonal pattern themselves. Because of the hexagonal pattern of the HTF tube distribution in each honeycomb heat exchanger bed, symmetry can be considered in the heat and mass transport processes. Due to this symmetry in heat and mass transport, a small element of the reactor

bed is considered in the present study (red dashed line in Fig. 1B). A three dimensional schematic of the computational domain is presented in Fig. 1C, where L_C is one edge of the hexagonal cell, δ_{fin} is the thickness of the hexagonal cell wall and R_{tube} is the radius of the HTF tube. The height of the computational domain is considered as half of the bed height because of the presence of symmetry in the heat and mass transfer at the center of each honeycomb heat exchanger bed as water vapor is transported from both sides of the bed. It is noted here with reference to Fig. 1C that the numerical simulations are carried out in a Cartesian coordinate system *x*, *y* and *z* because the system is not exactly cylindrical. However, the x-coordinate more or less corresponds to the radial position and the y-coordinate to the tangential position.

In the present study, the radius of the HTF tube is constant for all the cases and its value is taken 0.02 m. It is also assumed that the temperature gradient in the HTF flow direction is very small and can be neglected. The temperature at the internal surface of the HTF tube is set equal to the inlet temperature of HTF and its value is 30 ºC. The inlet of water vapor is considered at the top of the computational domain and the symmetry boundary at the bottom of the computational domain. At the top of the computational domain, the water vapor arrives with a fixed vapor concentration of 0.71 mol/m^3. This value is obtained based on water vapor properties as it is assumed that vapor is an ideal gas (hence we applied the gas law formula $\rho_v = M_v C$). The vacuum in the whole system is created at a pressure of around 1708 Pa. At t = 0, the concentration in the TCM bed equals 0.07 mol/m^3 and the initial temperature is set to 30 °C.

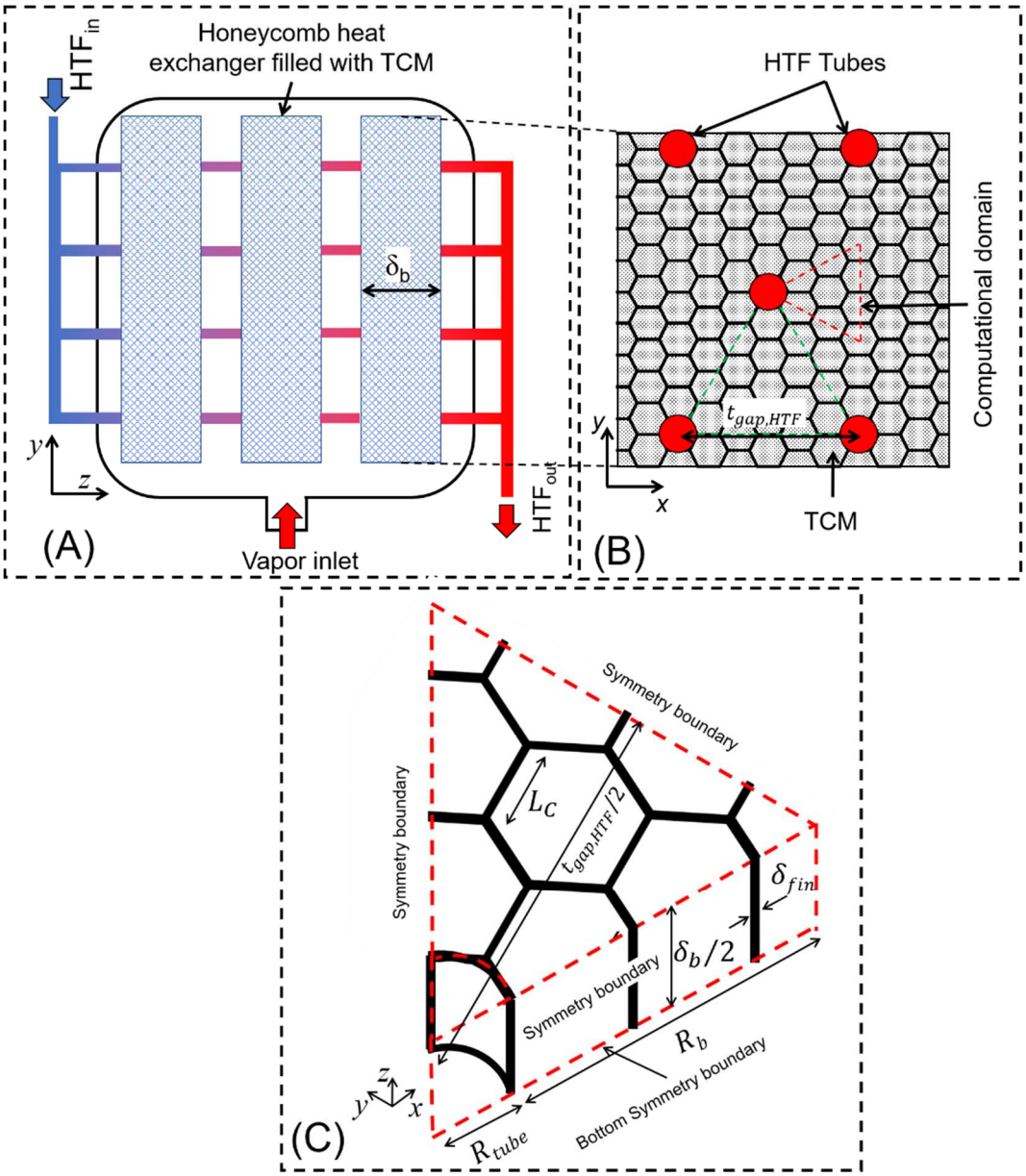

Fig. 1 Schematic of the geometry of the TCM bed and computational domain (a) TCM energy storage system, (b) side view of honeycomb heat exchanger filled with TCM, (c) computational domain.

3. GOVERNING EQUATIONS

3.1 VAPOR TRANSPORT IN POROUS MEDIUM

The vapor transport in the TCM filled in the honeycomb cells is governed by the mass conservation equation of the reactive gas and can be written as [42]:

$$\varepsilon_{eff}\frac{\partial C}{\partial t} - \nabla\cdot(D_v\nabla C) + \nabla\cdot(\boldsymbol{u}C) - R_C = 0 \quad (1)$$

where C and D_v are the concentration and the diffusion coefficient of the water vapor, respectively. ε_{eff} is the effective porosity and its value is taken 0.4 in the present study [41]. The last term (R_C) in eq. (1) is the reaction term which will be discussed in the reaction kinetics section. The vapor transport in the porous medium occurs not only from diffusion but also from advection, where a difference in pressure causes the bulk motion of the gas. This leads to a viscous flow and therefore the vapor transport in the porous medium is governed by Darcy's law considering the acceleration due to gravity. The Darcy velocity $\boldsymbol{u}$ in the porous medium is given by:

$$\boldsymbol{u} = -\frac{\kappa}{\mu}(\nabla p - \rho_v \vec{g}) \tag{2}$$

where ρ_v is water vapor density and g is universal gravitational constant. The p is the gas pressure and given by gas law ($p = CRT$, where C is the molar concentration, R is the universal gas constant and T is the temperature). The permeability κ of the porous medium can be obtained from the semi-empirical Blake–Kozeny equation as:

$$\kappa = \frac{d_p^2 \varepsilon_{eff}^2}{150(1-\varepsilon_{eff})^2} \tag{3}$$

where d_p is the particle diameter and ε_{eff} is the bed porosity. The Sutherland law or the viscosity-temperature relation is often used to determine the dynamic viscosity μ in the range of -156 [°C] to 1787 [°C], where the ratio S/T_{ref} is empirically taken as 0.505 [43].

$$\mu = \mu_{ref}\left(\frac{T}{T_{ref}}\right)^{\frac{1}{2}}\left\{\frac{1+\frac{S}{T_{ref}}}{1+\frac{S/T_{ref}}{T/T_{ref}}}\right\} \tag{4}$$

with T_{ref} and μ_{ref} as reference temperature and viscosity respectively.

3.2. HEAT TRANSFER IN POROUS MEDIUM

For the phases existing in the reactor bed, the macroscopic description of heat transfer in a porous medium is often investigated by the use of a single temperature equation. Here, local thermal equilibrium is referring to the fact that the macroscopic temperatures of the three phases (liquid water in the salt, water vapour in the reactive gas and the solid salt itself) are close enough such that a single temperature description of the heat transport processes can be

used. Duval et al. [44] added that the assumption of local thermal equilibrium was acceptable in many cases of unsaturated porous media with liquid–vapour phase change, particularly for most thermal decomposition processes. Therefore the heat transfer in the porous thermochemical bed is governed by the heat transfer diffusion equation, which can be written as [42]:

$$\left(\rho C_p\right)_{eff}\frac{\partial T}{\partial t} + \rho_v C_{p,v}\boldsymbol{u}\cdot\nabla T - k_{eff}\nabla^2 T = Q \tag{5}$$

where $\left(\rho C_p\right)_{eff}$ is the effective volumetric heat capacity, k_{eff} is the effective thermal conductivity and its value is considered $0.4\,W/mK$ in the present study [41]. The Q is the heat generated due to the reaction of water vapour with K_2CO_3 and its value depends on the reaction term R_c and will be discussed in the reaction kinetics section. The effective volumetric heat capacity $\left(\rho C_p\right)_{eff}$ is calculated by the following equation:

$$\left(\rho C_p\right)_{eff} = \rho_v C_{p,v}\varepsilon_{eff} + \rho_s C_{p,s}\left(1-\varepsilon_{eff}\right) \tag{6}$$

3.3. HEAT TRANSFER IN FIN

The heat transfer in the fin can be calculated with the heat transfer diffusion equation [45]:

$$\rho_{fin} C_{p,fin}\frac{\partial T}{\partial t} - k_{fin}\nabla^2 T = 0 \tag{7}$$

where ρ_{fin}, $C_{p,fin}$ and k_{fin} is the fin density, heat capacity and thermal conductivity respectively.

3.4. REACTION KINETICS

Solving the intra-particle mass balance equations is often time-consuming. To avoid this problem, in practice often a lumped approach is followed as an approximation, which has proven to be physically consistent [14,46]. The reaction term in equation (1) is calculated, using the reaction advancement:

$$R_c = \chi\,\frac{\rho_s}{M_s}\left(1-\varepsilon_{eff}\right)\frac{\partial \alpha}{\partial t} \tag{8}$$

where ρ_s is the density of the solid TCM, χ is the Stoichiometric coefficient, M_s is the molecular weight of potassium carbonate and α is the reaction advancement. Since reaction kinetics deals with measurement and parameterization of the process rates, the rate can be parameterized using three major variables: the temperature T, the chemical conversion α and the vapor pressure p. Systematic studies have been performed about the different expressions of the kinetic rates [15] in heterogeneous kinetics and the global form of that rate can be presented as follows:

$$\frac{\partial \alpha}{\partial t} = k(T) f(\alpha) h(p) \tag{9}$$

The value of the conversion α in time-dependence reflects typically the progress of the overall transformation of a reactant to products, meaning the advancement of the reaction. Lu et al. [47] (1996), Mazet et al. [48] had shown that the pressure dependence for reversible solid-gas synthesis can be expressed as:

$$h(p) = 1 - \left(\frac{p_{eq}}{p}\right) \tag{10}$$

where p and p_{eq} are the partial and equilibrium pressures of the gas product respectively (here the water vapour). The value of equilibrium vapour pressure $p_{eq}[Pa]$ is given by [22]:

$$p_{eq} = 4.228 \times 10^{12} exp\left(-\frac{7337}{T}\right) \tag{11}$$

where T is the temperature in K. The ratio between equilibrium water vapor pressure (p_{eq}) and water vapour pressure (p) called the pressure ratio ($\frac{p_{eq}}{p}$), is an important parameter in reaction kinetics. Assuming that mass transfer and chemical reaction are sufficiently rapid so that equilibrium values of concentrations always exist at prevailing temperature, the equation linking the equilibrium pressure to the temperature for the decomposition is given by the Clausius-Clapeyron relationship. For this type of reaction, several authors [5,47,48] have shown that the reaction rate can be presented as follows:

$$\frac{\partial \alpha}{\partial t} = A_f exp\left(-\frac{E_a}{RT}\right)(1-\alpha)^{2/3}\left(1 - \frac{p_{eq}}{p}\right) \tag{12}$$

where A_f is the pre-exponential Arrhenius factor taking into account the kinetic effect, E_a the Arrhenius activation energy. The source term Q in the eq. (8) is the heat generated or consumed in adsorber bed which is given by:

$$Q = R_c \Delta H_r \tag{20}$$

where R_c is the reaction rate as introduced previously and ΔH_r is the reaction enthalpy (given in table 1).

3.5. INITIAL AND BOUNDARY CONDITIONS

The following boundary conditions are prescribed, see Fig. 1C:

- At the top of the computational domain, the water vapour pressure is fixed.
- At the bottom of the computational domain, the symmetry boundary condition is applied, for temperature and gas flux.
- At the surface of the honeycomb heat exchanger, the velocity field is zero ($-n\nabla u = 0$), there are heat continuity between porous TCM and honeycomb fin, therefore ($-nk_{eff}\nabla T = -nk_{fin}\nabla T$).
- At the HTF tube inner surface, a constant temperature boundary condition is applied ($T = T_{HTF}$).
- At the periphery (other than the HTF boundary) of the computational domain, the symmetry boundary condition is applied.

Initially, the temperature of the computational domain was ($T_i = 30^o C$) and the reaction advancement of the bed is fixed at zero (α = 0). The initial pressure is fixed at 425 Pa corresponding initial water vapor concentration is 0.07 mol/m^3.

3.6. COMPUTATIONAL PROCEDURE AND MODEL VALIDATION

The governing partial differential equations subjected to initial and boundary conditions are simultaneously solved using the commercial package of COMSOL Multiphysics 5.3a, which is based on the Finite Element Method (FEM). The expressions for the thermophysical properties of TCM and reaction kinetics are programmed in COMSOL through user-defined functions. The partial differential equations for heat and mass transport are programmed in the 'heat transfer in porous media' and 'transport of diluted species in porous media'

311 interfaces available in COMSOL [49]. With respect to the 3-dimensional model for the heat
312 and mass transport study, free meshing with tetrahedral elements is used to create the overall
313 mesh. The numerical simulation model is divided into two calculation domains i.e. the solid
314 and the porous domain and each discretized using the Galerkin method. The mesh size and
315 time step dependencies of the solutions are studied to check the accuracy of the numerical
316 results and computation time. It was optimized with three progressive decreasing mesh sizes
317 and final values are taken because further reducing mesh size did not significantly affect the
318 final results. The mesh size was decreased near the interfaces of the solid with the porous
319 medium to reduce the error in the calculations. The maximum and minimum mesh element
320 size considered in the present study is 0.0013 m and 0.000132 m which is small enough to
321 obtain accurate mesh independent solutions. An independent discretization of the time
322 domain is applied using the method of lines and time-stepping algorithms automatically
323 switch between explicit and implicit steps depending on the problem. The time step may vary
324 in order and step length depending on the evolution of the solution with time. The maximum
325 time step is defined as 1 min, however, at the initial stage of convergence, the time step is
326 taken very small by the solver, in the order of 10^{-3} seconds.

327 The numerical model for heat and mass transport in the porous medium as used in the present
328 study is based on a model developed in our lab for the hydration of silica gel. First, the
329 kinetics of silica gel is replaced with the kinetics of potassium carbonate, and then the heat
330 transfer model for the honeycomb heat exchanger is added. The developed model for the
331 reaction kinetics is validated with experimental results presented by Gaeini et al. [22] in
332 terms of reaction advancement, see Fig. 2. In the experiments, the hydration isotherm is kept
333 at 30 ^{o}C and hydration starts only when water vapor is introduced to the system while the
334 isotherm temperature is maintained. The water vapor pressure was maintained at 1715 Pa.
335 More details can be found in Gaeini et al. [22]. The comparative results present the validity of
336 the developed model as results from the present study are in good agreement with the
337 experimental results obtained by Gaeini et al. [22]. However, a minor shift compared to the
338 experimental data is observed. This can be explained by a possible difference in some
339 thermo-physical properties (effective thermal conductivity and effective porosity) of the
340 porous K_2CO_3 sample as these values are not presented by Gaeini et al. [22]. In the present
341 work, these properties are taken from the literature [41].

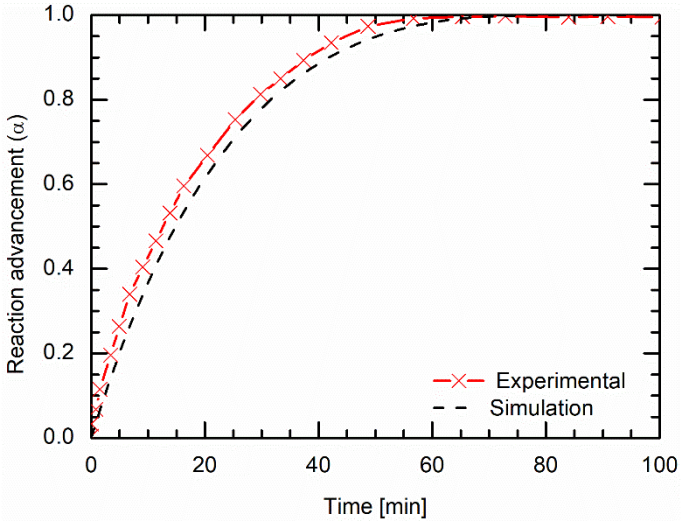

Fig. 2 Comparison of reaction advancement with experimental study of Gaeini et al. [22]

4. RESULTS AND DISCUSSION

The present study is conducted for the hydration of K_2CO_3 and the obtained results of the study are presented in two subsections. The initial and boundary conditions considered in the present study are listed in Table 1 and section 3.5. In the first subsection the heat transfer, reaction advancement and reaction rate are being discussed. In the second subsection, the results of the parametric study for different cell sizes (L_C), bed heights (δ_b), fin thickness (δ_{fin}) and the distance between two HTF tubes ($t_{HTF,gap}$) are discussed.

4.1. HEAT TRANSFER, REACTION ADVANCEMENT AND REACTION RATE

Figure 3 presents the temperature contour of the computational domain (i.e. TCM bed with honeycomb heat exchanger) at 5 min, 15 min, 30 min, 60 min, 90 min and 120 min considering $L_c = 0.01\ m, \delta_b/2 = 0.015\ m, \delta_{fin} = 0.001\ m\ and\ t_{gap,HTF}/2 = 0.090\ m$. For the given configuration, the actual volume of the porous K_2CO_3 sample is 52.43 cm^3 and the ratio of the porous bed to fin volume is 3.6. From Figure 3, it can be observed that the temperature in the computational domain for each time span is increasing with an increase in the distance from the HTF tube and also increases towards the center of each hexagonal cell of the honeycomb heat exchanger. Further, the temperature is higher at the top of the computational domain and starts decreasing with an increase in the distance from the top of the bed as the concentration of the water vapour is progressively decreasing with an increase in the distance which results in a reduced heat generation in the bed. The temperature

distribution in each hexagonal cell is not perfectly symmetric; its maximum value is slightly shifted away from the HTF tube. The temperature distribution in the y-direction of the bed (comparable to the tangential direction in cylindrical coordinates) is almost periodic because of symmetry in the hexagonal fin structure of the honeycomb.

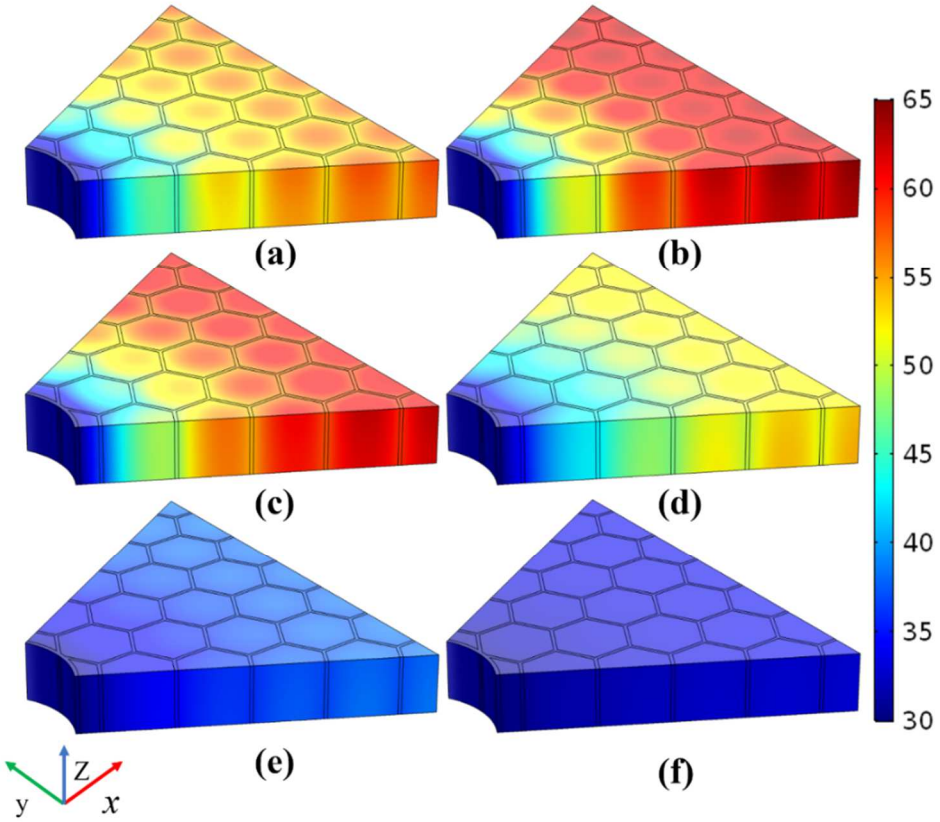

Fig.3 Colour contour of the temperature of TCM bed at different time levels (a) 5 min, (b) 15 min, (c) 30 min, (d) 60 min, (e) 90 min, (f) 120 min

Further, the temperature variations with time at different probe points in the computational domain are shown in Fig. 4. The probe points P1 to P5 are equally spaced at a distance of 0.02 m in the x-direction (radial direction) starting from the HTF tube and P5 to P8 are positioned at the center of each hexagonal cell and also space at an equal distance of 0.01732 m in the y-direction (tangential direction) from probe point P5. Further, all the probe points are positioned at the half-thickness of the computational domain ($z = \delta_b/4$).

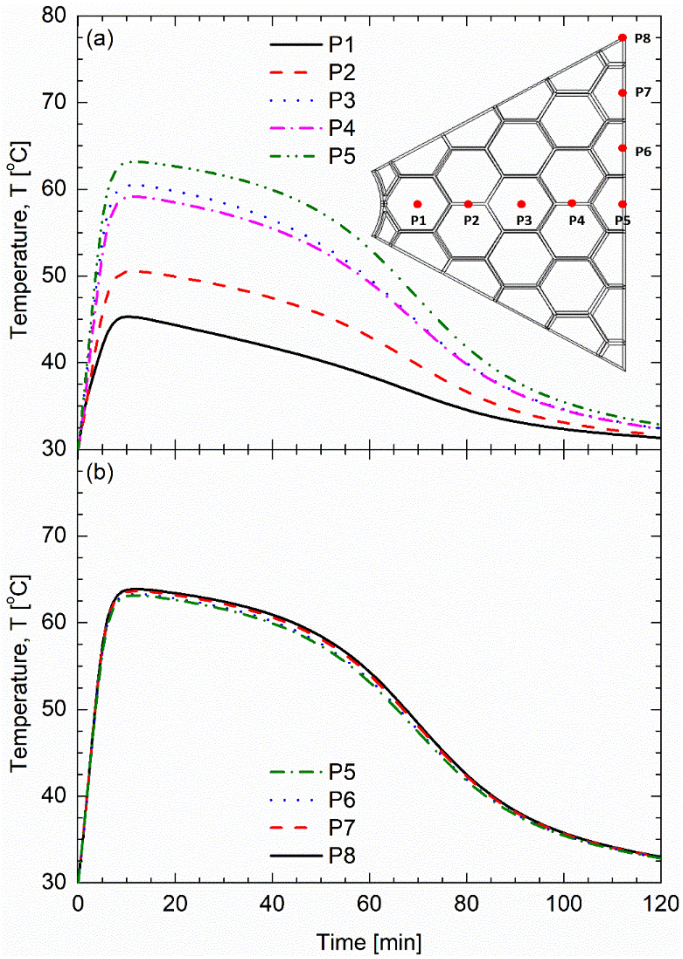

Fig. 4 Temperature variation at the different probe points (a) in the x-direction (radial direction), (b) in the y-direction (tangential direction)

Fig. 4 shows the honeycomb heat exchanger bed temperature variation at the above-discussed probe points (i.e. P1 to P8). The temperature of the bed at all probe points is increasing sharply at the initial stage of reaction and reaches its maximum value at around 10 min, further it starts decreasing gradually. Fig. 4(a) represents the variation of bed temperature with time at probe point P1 to P5. The minimum temperature is observed at probe point P1 as it is nearest to the HTF tube. The temperature of the bed is increasing with an increase in distance from the HTF tube, though, the temperature at probe point 4 is lower than P3 as P4 is positioned in the honeycomb fin and P3 is placed in the center of the hexagonal cell. Fig 4(b) represents the variation of temperature at different probe points (P5 to P8) in the y-direction (tangential direction). The temperature difference in probe points P5 to P8 is very small because of the presence of the honeycomb fin structure and symmetry considerations.

Fig 5 presents the variation of reaction advancement (α, eq. (12)) and reaction rate (R_c, Eq. (8)) of water vapor with K_2CO_3 at different probe points with time. The positions of probe

393 points are presented above. Because the probe points P2 and P4 coincide with the fin
394 structure, they are left out of this analysis. Up to 55 min, the reaction advancement is the
395 highest at probe point P1, from 55 min onwards probe point P3 shows the highest reaction
396 advancement, as shown in Fig. 5(a). Minimum reaction advancement is obtained at probe
397 point P8 because it is the furthest probe point from the HTF tube in the thermochemical
398 reactor bed. The decreasing order of reaction advancement at different probe points before
399 and after 55 min is P1>P3>P5>P6>P7>P8 and P3>P1>P5>P6>P7>P8 respectively. It should
400 be noted however that the values for reaction advancement are quite close to each other for
401 the points P5-P8 over the full-time interval. This applies to all points for times greater than 80
402 min. Besides, the reaction rate of water vapour with K_2CO_3 at the different probe, points are
403 shown in Fig. 5(b). Initially, the reaction rate increases sharply and reaches its maximum
404 value for all probe points and then it starts decreasing with different proportions. At probe
405 point P1, the reaction rate continuously decreases after getting its maximum value, though,
406 for other probe points, the reaction rate sharply decreases with time until reaches its
407 minimum value (≈ t = 10 min). After reaching the minimum value of reaction rate it further
408 starts increasing with time up to ≈ 35 min for P3 and t = ≈ 55 min for P5, P6, P7, P8. This can
409 be explained as the water vapour seeps into the bed and reacts with TCM, which results in the
410 temperature rise in the bed. The temperature rise in the bed causes a reduction in the reaction
411 rate.

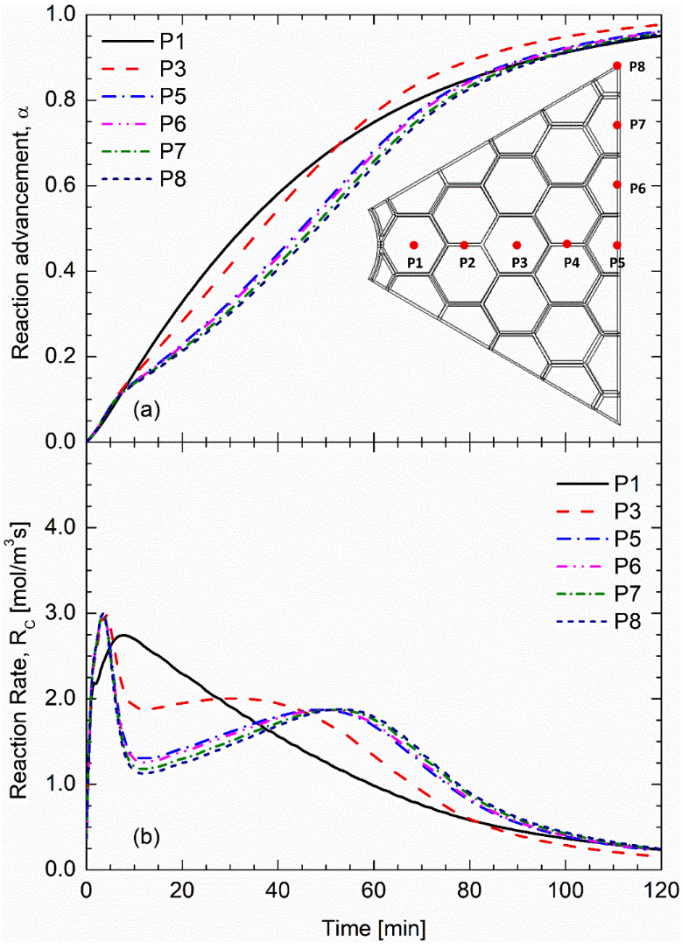

Fig. 5 Variation of (a) reaction advancement, (b) Reaction rate at the different probe points with time

4.2. PARAMETRIC STUDY

Below a discussion on the results obtained from a parametric study of honeycomb cell size, bed height, honeycomb fin thickness and the distance between two HTF tubes are presented. The results are presented in terms of temperature variation (T), reaction advancement (α) and power output (P_o). The power output P_o is obtained by integrating the heat flux over the HTF tube surface and is defined as:

$$P_o = \oiint \vec{q} dS$$

with the heat flux $\vec{q}$ integrated over the surface S of the HTF tube.

4.2.1. Effect of honeycomb cell size

Fig. 6 shows the temperature contours of the computational domain for four different honeycomb cell sizes i.e. L_C = 0.005 m, 0.01 m, 0.015 m, and 0.02 m at 15 min. The default values of $\delta_b/2$, δ_{fin} and $t_{gap,HTF}/2$ for all the cell sizes are 0.015 m, 0.001 m, and 0.09 respectively. The volumes of the porous K_2CO_3 samples for L_C = 0.005 m, 0.01 m, 0.015 m, and 0.02 m are 52.43 cm^3, 59.49 cm^3, 61.95 cm^3 and 63.20 cm^3 respectively. Further, the volume ratios of the porous K_2CO_3 samples with respect to the metallic fin volumes are 3.6, 7.9, 12.25 and 16.57 respectively. The smaller honeycomb cell size increases the number of cells in the TCM bed and consequently also increases the fin material volume. The increment of the fin volume in the computational domain causes enhanced heat transport in the bed; however, it reduced the actual heat capacity of the bed. The temperature gradient in the computational domain is lowest for the smallest cell size of the honeycomb structure and vice versa, because of better heat transport from the TCM bed to the HTF.

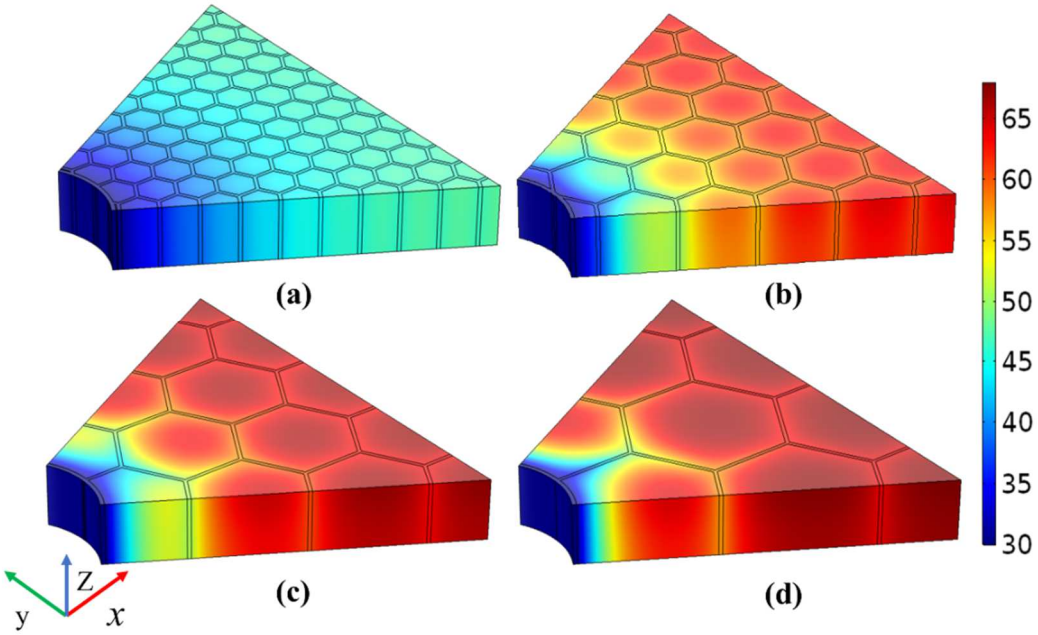

Fig. 6 Temperature contours at different cell sizes (a) L_C = 0.005 m, (b) L_C = 0.01 m, (c) L_C = 0.015 m, (d) L_C = 0.02 m at 15 min

Further, the temperature variation, reaction advancement and thermal power transported to the HTF with time are plotted in Fig. 7 at probe point 8 (as shown in fig 5a). The temperature at probe point P8 (the point furthest away from the HTF tube) increases sharply for all the

cell sizes and gradually starts decreasing after reaching its maximum value as shown in Fig 7(a). For the lowest cell size (L_C = 0.005 m), the maximum temperature at probe point P8 reaches 47 °C after 10 min. Further, the temperature gradually starts decreasing and reaches the lowest value of 32 °C at 120 min. For L_C = 0.01 m, the temperature at probe point P8 sharply reaches its maximum value and starts decreasing gradually until 60 min. Further, it sharply decreases and becomes 32 °C after 120 min. Fig. 7(b) shows the reaction advancement at probe point P8 for all cell sizes. For L_C = 0.005 m and L_C = 0.01 m, the reaction advancement at 120 min reaches around 0.95 however for L_C = 0.015 m and L_C = 0.02 m its value is 0.8 and 0.35 respectively.

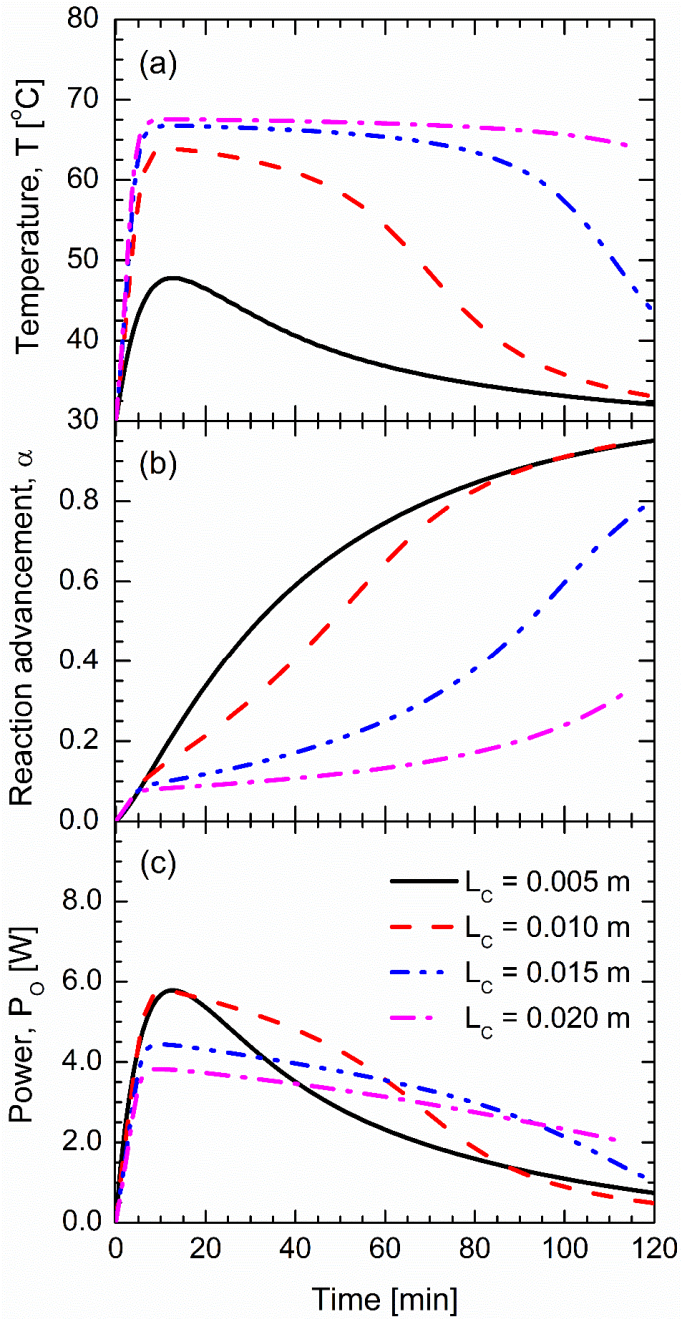

Fig. 7 Variation of (a) Temperature, (b) reaction advancement and (c) power output with time for different cell sizes; temperature and reaction advancement are presented for probe point P8

The lowest reaction advancement is obtained with the highest cell size because of the higher temperature which causes a reduced reaction rate of water vapour with K_2CO_3. Fig. 7 (c) presents the variation of power output with time at the HTF tube surface in the computational domain. The power output (P_O) reaches its maximum value at the same time when the temperature at probe point P8 is maximum. For L_C = 0.015 m and L_C = 0.02 m, there is a gradual reduction in power output after reaching its maximum value, however, it is sharper for L_C = 0.005 m and L_C = 0.01 m. The smaller honeycomb cell size leads to a higher number of cells in the computational domain which reduces the actual volume of the reacting material in the computational domain. The reduction in the volume of reacting material reduces the heat storage capacity of the reacting bed.

4.2.2. Effect of bed height

The temperature contours of the computational domain for four different bed height ($\delta_b/2 = 0.005\,m$, $\delta_b/2 = 0.01\,m$, $\delta_b/2 = 0.015\,m$, and $\delta_b/2 = 0.02\,m$) at 15 min are presented in Fig. 8. The fin thickness, honeycomb cell size and the distance between two HTF tubes are considered 0.001 m, 0.01m and 0.09 m respectively. The volumes of the porous K_2CO_3 samples for $\delta_b/2 = 0.005\,m$, $\delta_b/2 = 0.01\,m$, $\delta_b/2 = 0.015\,m$, and $\delta_b/2 = 0.02\,m$ are 19.83 cm^3, 39.66 cm^3, 59.49 cm^3 and 79.32 cm^3 respectively. The ratio of the porous K_2CO_3 sample volume to the metallic fin volume is fixed at 7.9. At 15 min, the temperature gradient in the computational domain is almost the same for all bed heights (Fig. 8 (a)-(d)), however, its value is slightly higher for the computational domain with the lowest bed height as compared to the higher bed height (Fig. 9). For the smaller bed height, the water vapour easily seeps into the bed and reacts with the TCM, which enhances the reaction rate and results in a higher temperature.

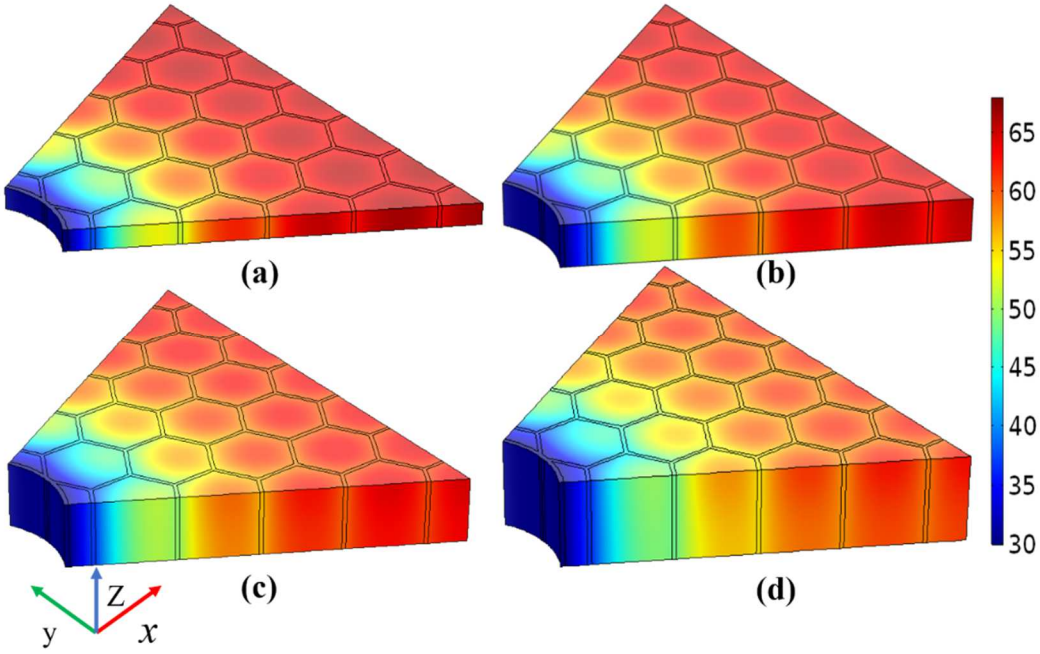

480

481 Fig. 8 Temperature contours at different bed height (a) $\delta_b/2 = 0.005\ m$, (b) $\delta_b/2 = 0.01\ m$,

482 (c) $\delta_b/2 = 0.015\ m$, (d) $\delta_b/2 = 0.02\ m$ at t=15 min

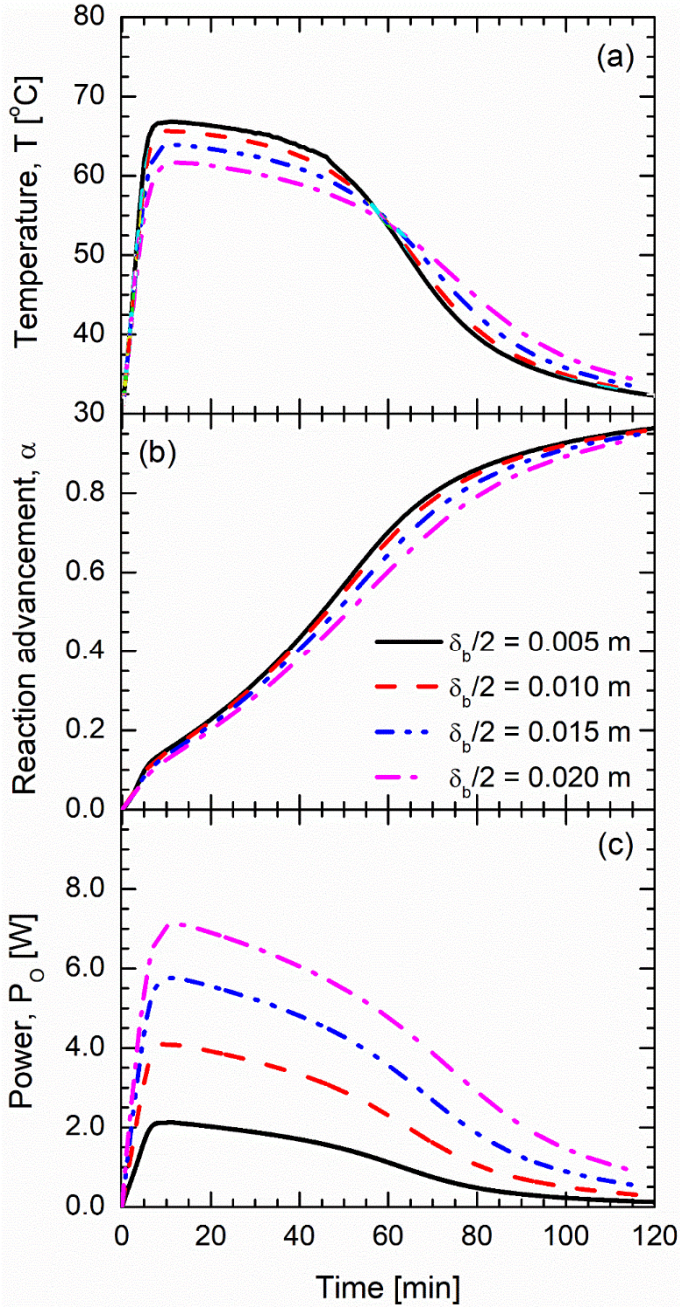

Fig. 9 Variation of (a) Temperature, (b) reaction advancement and (c) power output with time for different cell sizes; temperature and reaction advancement are presented for probe point P8

The temperature at probe point P8 (discussed in the previous section) is presented in Fig 9 (a) for different bed thicknesses. At this probe point the bed temperature is higher for the lowest bed thickness until t = 60 min and vice versa after 60 min. Further, reaction advancement is always higher for the lowest bed height (i.e. $\delta_b/2 = 0.005\,m$) because of the lower flow resistance and lower uptake of vapor in the bed which results in better accessibility of and higher concentration in the computational domain. Further, the power output from the

computational domain to the HTF surface is presented in Fig. 9(c). The maximum power is obtained with the maximum bed thickness simply because of the presence of more TCM in the computational domain. However, it is interesting to see that the power output is linearly increasing with the bed height for the 2 smaller values ($\delta_b/2 = 0.005\,m$ and $\delta_b/2 = 0.01\,m$) but slightly decreases for the 2 larger values ($\delta_b/2 = 0.015\,m$ and $\delta_b/2 = 0.02\,m$). There is a progressive attenuation in power with time for higher bed height because the fraction of hydrated TCM increases and subsequently reduce the reactant volume with time, which results in lower power production.

4.2.3. Effect of honeycomb fin thickness

The temperature variation of the computational domain for four different fin thicknesses ($\delta_{fin} = 0.0005\,m$, $\delta_{fin} = 0.001\,m$, $\delta_{fin} = 0.0015\,m$, and $\delta_{fin} = 0.002\,m$) at 15 min are presented in Fig. 10 considering L_C = 0.01 m, $\delta_b/2 = 0.015\,m$ and $T_{\,gap,HTF}/2 = 0.09\,m$. The volumes of the porous K2CO3 samples for $\delta_{fin} = 0.0005\,m$, $\delta_{fin} = 0.001\,m$, $\delta_{fin} = 0.0015\,m$, and $\delta_{fin} = 0.002\,m$ are 63.19 cm^3, 59.49 cm^3, 55.90 cm^3 and 52.43 cm^3 respectively. Further, the ratios of the porous K2CO3 sample volumes to the metallic fin volumes are 16.57, 7.92, 5.03 and 3.60 respectively. The highest temperature gradient in the TCM bed is observed with the lowest fin thickness due to the reduction in the thermal transport from the bed to the HTF surface (increased heat resistance because of a reduced cross-sectional area of the fin structure). Further, the increment in the fin thickness also reduces the actual volume of the TCM in the bed, which also results in reduced heat generation and causes a lower bed temperature.

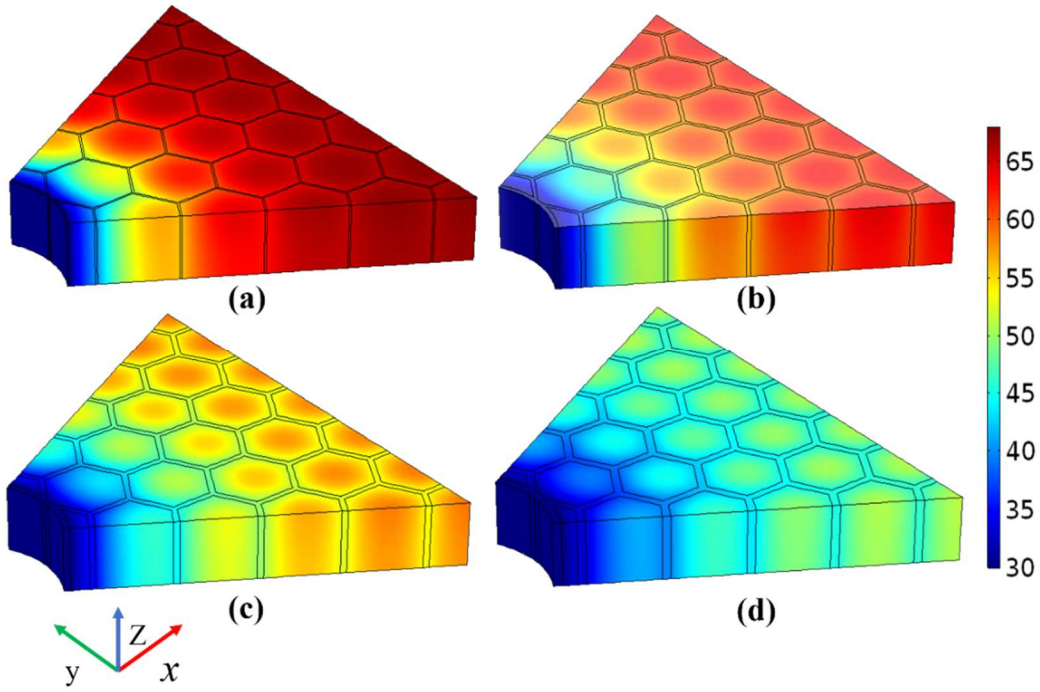

515

516 Fig. 10 Temperature contours at different honeycomb fin thickness (a) $\delta_{fin} = 0.0005\ m$, (b)

517 $\delta_{fin} = 0.001\ m$, (c) $\delta_{fin} = 0.0015\ m$, (d) $\delta_{fin} = 0.002\ m$ at t=15 min

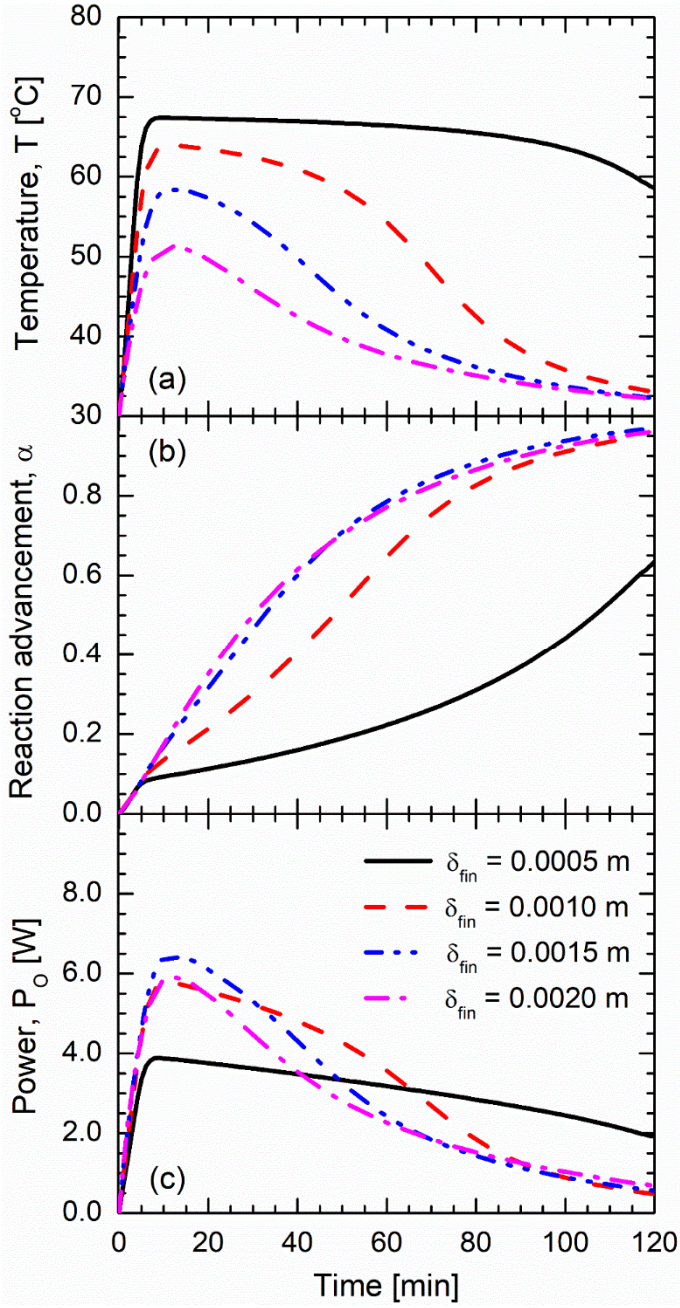

518

519 Fig. 11 Variation of (a) Temperature, (b) reaction advancement and (c) power output with
520 time for different cell sizes; temperature and reaction advancement are presented for probe
521 point P8

Further, the temperature variation, reaction advancement at probe point P8 and power output from the computational domain are presented in Fig 11 (a), Fig. 11(b) and Fig. 11 (c) respectively. The temperature for the minimum fin thickness is the highest and, vice versa, the temperature for the maximum fin thickness is the lowest which is understandable because it influences the thermal transport from the bed to the HTF as discussed above. For $\delta_{fin} = 0.001\,m$, $\delta_{fin} = 0.0015\,m$, and $\delta_{fin} = 0.002\,m$ the temperature at 120 min reaches to 32 ^{o}C, slightly above its initial value of 30 ^{0}C, however for $\delta_{fin} = 0.0005\,m$ its value is still around 59 ^{o}C because the hydration reaction is still in full swing as can be concluded from the reaction advancement. The reaction advancement at probe point P8 is presented in Fig. 11 (b). From Fig. 11(b) it is observed that the reaction advancement reached around 0.98 at 120 min, for the fin thickness greater than 0.0005 m, however, it reaches 0.68 for fin thickness 0.0005 m. The power output from the TCM bed is presented in Fig. 11(c). Initially, the power output sharply increases and starts decreasing gradually after reaching its peak value. The maximum peak power is obtained for fin thickness $\delta_{fin} = 0.0015\,m$, the minimum peak power for fin thickness of $\delta_{fin} = 0.0005\,m$. In Fig. 11 (c) it is also observed that the power output with $\delta_{fin} = 0.002\,m$ fin thickness is lower as compared to $\delta_{fin} = 0.0015\,m$ because a larger fin thickness results in a larger volume of fin material and reduces the actual volume of the TCM which causes lower power output. Finally, it is interesting to note that for a lower fin thickness the peak power goes down but the power is more constant over time than for a higher fin thickness.

4.2.4. Effect of distance between two HTF heat pipe

Numerical simulations have also been conducted to see the effect of the distance between two HTF tube ($t_{gap,HTF}$). The simulations have been performed for $t_{gap,HTF}/2 = 0.045\,m$, $t_{gap,HTF}/2 = 0.090\,m$, and $t_{gap,HTF}/2 = 0.135\,m$. The volumes of the porous K_2CO_3 samples for $t_{gap,HTF}/2 = 0.045\,m$, $t_{gap,HTF}/2 = 0.090\,m$, and $t_{gap,HTF}/2 = 0.135\,m$ are 12.78 cm^3 59.49 cm^3 and 137.34 cm^3 respectively and the ratio of the porous K_2CO_3 samples to the metallic fins volume is fixed at 7.92. The obtained temperature contours at 15 min are presented in Fig. 12(a), Fig. 12(b) and Fig. 12(c) respectively. The temperature gradient near the HTF tube in the computational domain is smaller for a smaller distance between two HTF tubes. The temperature gradient in each cell near the HTF tube is also higher for the higher $t_{gap,HTF}/2$. For maximum $t_{gap,HTF}/2$, when moving away from the HTF tube the

553 temperature gradient in each cell starts decreasing. At the maximum distance from the HTF
554 tube, the temperature gradient is negligible. Further, temperature variation and reaction
555 advancement at probe point 8 and power output from the TCM bed is presented in Fig 13(a),
556 Fig. 13(b) and Fig. 13(c) respectively. It is evident that for higher values of $t_{gap,HTF}/2$ the
557 temperature at probe point 8 is the highest. For $t_{gap,HTF}/2 = 0.045$ m and 0.09m, the
558 temperature increases to its maximum value and then it starts decreasing. For minimum
559 $t_{gap,HTF}/2$ (0.045 m), the maximum temperature reaches 37.5 ºC at around 5 min and starts
560 decreasing gradually with time and reaches 31 ºC at 120 min. For maximum $t_{gap,HTF}/2$
561 (0.135 m), the temperature reaches 68 ºC at 10 min and its value remains around 68 ºC over
562 the whole time span. From the reaction advancement as presented in Fig. 13(b), it is observed
563 that the reaction advancement is higher for the lowest $t_{gap,HTF}/2$ in the initial stage of
564 reaction and becomes maximum for $t_{gap,HTF}/2 = 0.09\,m$ after 60 min. Further, the power
565 output of the TCM bed is also presented in Fig. 13 (c) for different $t_{gap,HTF}/2$ values. For all
566 its values the power output increases in precisely the same way. However, the smaller the
567 $t_{gap,HTF}/2$ value, the earlier the maximum is reached. The maximum power output is
568 achieved with the highest $t_{gap,HTF}/2$ because of the higher volume of the TCM bed.
569

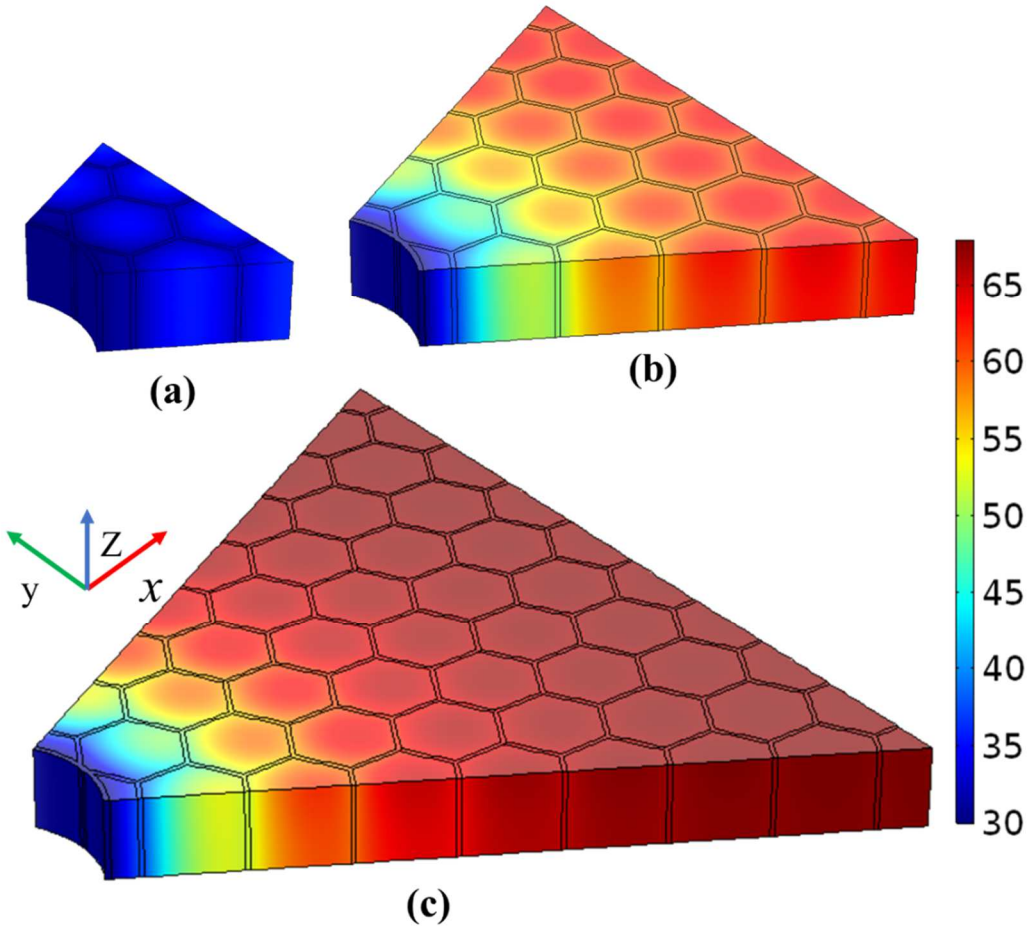

570

571 Fig. 12 Temperature contours for different distance values between two HTF tubes

572 (a) $\frac{t_{gap,HTF}}{2} = 0.045\ m$, (b) $\frac{t_{gap,HTF}}{2} = 0.090\ m$, (c) $\frac{t_{gap,HTF}}{2} = 0.135\ m$ at t=15 min

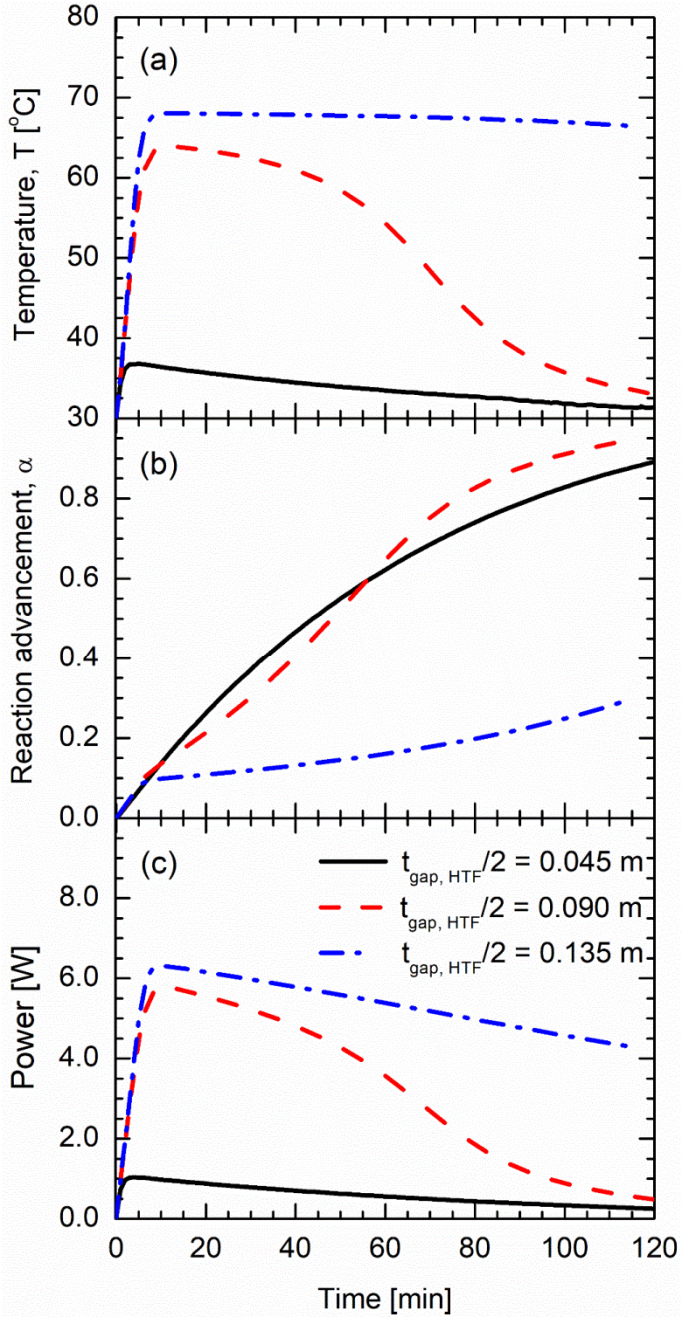

Fig. 13 Variation of (a) Temperature, (b) reaction advancement and (c) power output with time for different distances between two HTF tubes; temperature and reaction advancement are presented for probe point P8

5. CONCLUSIONS

A thermochemical energy storage system using potassium carbonate and water as the sorbent/sorbate reaction pair ($K_2CO_3/K_2CO_3.1.5H_2O$) is studied numerically considering a three-dimensional fixed honeycomb heat exchanger bed filled with K_2CO_3-particles. The

thermochemical bed is cooled from the center of the honeycomb heat exchanger by an HTF flow. The developed numerical model for the reaction kinetics of potassium carbonate is validated with experimental data in terms of reaction advancement. The results obtained provide detailed insight into the temperature variation and reaction propagation in the reactive solid TCM bed during discharging. A parametric study has been conducted to see the effect on the heat transfer of the honeycomb cell size, the bed height, the honeycomb fin thickness and the distance between two HTF tubes. It is concluded that an increase in bed height, cell size and fin thickness affect the discharge process to a great extent. Increasing the height of the bed will restrict the vapor flow within the bed whereas increasing the cell size and decreasing the fin thickness of the honeycomb heat exchanger will reduce the heat transfer to/from the bed due to poor conductivity properties. Increasing the distance between two HTF tubes will result in an increase of the temperature maximum and, therefore, will require heat transfer enhancement techniques if this temperature must remain below a certain value (to avoid dehydration during hydration for example).

It can be concluded that the developed numerical model is a very powerful tool in predicting all details of the physical phenomena taking place in the three-dimensional fixed honeycomb heat exchanger bed packed with K_2CO_3-particles. The model is also well suited for other applications utilizing different TCMs and different heat exchanger configurations. Changes in temperature, reaction advancement and power output with respect to geometry can easily be investigated using a similar approach. The next step is the design and the test of a prototype of the most optimal storage system equipped with honeycomb heat exchangers at a significant scale. The test of this prototype will allow us to demonstrate the feasibility of the potassium carbonate seasonal thermochemical storage process with a fixed bed honeycomb heat exchanger configuration functioning with water vapor for the built environment.

Acknowledgments

This research has been made possible by the Energy Pads program, funded by TKIenergo and work is done in cooperation with ArtEnergy and De Beijer RTB Stenograaf 1, 6921 EX Duiven, Netherlands.

609 **References**

610 [1] E.U. Commission, Clean energy for all Europeans package | Energy, European
611 Commission. (2019). https://ec.europa.eu/energy/en/topics/energy-strategy/clean-
612 energy-all-europeans (accessed July 2, 2020).

613 [2] E.U. Commission, An EU Strategy on Heating and Cooling, European Commission.
614 (2019). https://ec.europa.eu/energy/topics/energy-efficiency/heating-and-
615 cooling_en?redir=1 (accessed July 3, 2020).

616 [3] M. Hamidi, V.M. Wheeler, X. Gao, J. Pye, K. Catchpole, A.W. Weimer, Reduction of
617 iron–manganese oxide particles in a lab-scale packed-bed reactor for thermochemical
618 energy storage, Chemical Engineering Science. 221 (2020) 115700.
619 https://doi.org/10.1016/j.ces.2020.115700.

620 [4] X. Peng, M. Yao, T.W. Root, C.T. Maravelias, Design and analysis of concentrating
621 solar power plants with fixed-bed reactors for thermochemical energy storage, Applied
622 Energy. 262 (2020) 114543. https://doi.org/10.1016/j.apenergy.2020.114543.

623 [5] B. Michel, N. Mazet, S. Mauran, D. Stitou, J. Xu, Thermochemical process for
624 seasonal storage of solar energy: Characterization and modeling of a high density
625 reactive bed, Energy. 47 (2012) 553–563.
626 https://doi.org/10.1016/j.energy.2012.09.029.

627 [6] M. Hamidi, V.M. Wheeler, P. Kreider, K. Catchpole, A.W. Weimer, Effective thermal
628 conductivity of a bed packed with granular iron–manganese oxide for thermochemical
629 energy storage, Chemical Engineering Science. 207 (2019) 490–494.
630 https://doi.org/10.1016/j.ces.2019.06.035.

631 [7] S. Funayama, H. Takasu, S.T. Kim, Y. Kato, Thermochemical storage performance of
632 a packed bed of calcium hydroxide composite with a silicon-based ceramic
633 honeycomb support, Energy. 201 (2020) 117673.
634 https://doi.org/10.1016/j.energy.2020.117673.

635 [8] M. Wokon, A. Kohzer, M. Linder, Investigations on thermochemical energy storage
636 based on technical grade manganese-iron oxide in a lab-scale packed bed reactor, Solar

637 Energy. 153 (2017) 200–214. https://doi.org/10.1016/j.solener.2017.05.034.

638 [9] M. Schmidt, A. Gutierrez, M. Linder, Thermochemical energy storage with
639 CaO/Ca(OH)2– Experimental investigation of the thermal capability at low vapor
640 pressures in a lab scale reactor, Applied Energy. 188 (2017) 672–681.
641 https://doi.org/10.1016/j.apenergy.2016.11.023.

642 [10] V. Mamani, A. Gutiérrez, S. Ushak, Development of low-cost inorganic salt hydrate as
643 a thermochemical energy storage material, Solar Energy Materials and Solar Cells. 176
644 (2018) 346–356. https://doi.org/10.1016/j.solmat.2017.10.021.

645 [11] A. Fopah Lele, F. Kuznik, H.U. Rammelberg, T. Schmidt, W.K.L. Ruck, Thermal
646 decomposition kinetic of salt hydrates for heat storage systems, Applied Energy.
647 (2015). https://doi.org/10.1016/j.apenergy.2015.02.011.

648 [12] C.C.M. Rindt, S. V. Gaastra-Nedea, Modeling thermochemical reactions in thermal
649 energy storage systems, in: Advances in Thermal Energy Storage Systems: Methods
650 and Applications, 2015. https://doi.org/10.1533/9781782420965.3.375.

651 [13] A. Fopah Lele, K.E. N'Tsoukpoe, T. Osterland, F. Kuznik, W.K.L. Ruck, Thermal
652 conductivity measurement of thermochemical storage materials, Applied Thermal
653 Engineering. 89 (2015) 916–926.
654 https://doi.org/10.1016/j.applthermaleng.2015.06.077.

655 [14] A. Fopah-Lele, F. Kuznik, T. Osterland, W.K.L. Ruck, Thermal synthesis of a
656 thermochemical heat storage with heat exchanger optimization, Applied Thermal
657 Engineering. 101 (2016) 669–677.
658 https://doi.org/10.1016/j.applthermaleng.2015.12.103.

659 [15] A. Fopah Lele, A Thermochemical Heat Storage System for Households, Springer
660 International Publishing, Cham, 2016. https://doi.org/10.1007/978-3-319-41228-3.

661 [16] E. Karasavvas, K.D. Panopoulos, S. Papadopoulou, S. Voutetakis, Energy and exergy
662 analysis of the integration of concentrated solar power with calcium looping for power
663 production and thermochemical energy storage, Renewable Energy. 154 (2020) 743–
664 753. https://doi.org/10.1016/j.renene.2020.03.018.

665 [17] K.E. N'Tsoukpoe, T. Osterland, O. Opel, W.K.L. Ruck, Cascade thermochemical
666 storage with internal condensation heat recovery for better energy and exergy
667 efficiencies, Applied Energy. 181 (2016) 562–574.
668 https://doi.org/10.1016/j.apenergy.2016.08.089.

669 [18] X. Zhou, M. Mahmood, J. Chen, T. Yang, G. Xiao, M.L. Ferrari, Validated model of
670 thermochemical energy storage based on cobalt oxides, Applied Thermal Engineering.
671 159 (2019) 113965. https://doi.org/10.1016/j.applthermaleng.2019.113965.

672 [19] S. Tescari, C. Agrafiotis, S. Breuer, L. de Oliveira, M.N. Puttkamer, M. Roeb, C.
673 Sattler, Thermochemical Solar Energy Storage Via Redox Oxides: Materials and
674 Reactor/Heat Exchanger Concepts, Energy Procedia. 49 (2014) 1034–1043.
675 https://doi.org/10.1016/j.egypro.2014.03.111.

676 [20] P. Pardo, A. Deydier, Z. Anxionnaz-Minvielle, S. Rougé, M. Cabassud, P. Cognet, A
677 review on high temperature thermochemical heat energy storage, Renewable and
678 Sustainable Energy Reviews. 32 (2014) 591–610.
679 https://doi.org/10.1016/j.rser.2013.12.014.

680 [21] Q. Ranjha, A. Oztekin, Numerical analyses of three-dimensional fixed reaction bed for
681 thermochemical energy storage, Renewable Energy. 111 (2017) 825–835.
682 https://doi.org/10.1016/j.renene.2017.04.062.

683 [22] M. Gaeini, S.A. Shaik, C.C.M. Rindt, Characterization of potassium carbonate salt
684 hydrate for thermochemical energy storage in buildings, Energy and Buildings. 196
685 (2019) 178–193. https://doi.org/10.1016/j.enbuild.2019.05.029.

686 [23] L.C. Sögütoglu, P.A.J. Donkers, H.R. Fischer, H.P. Huinink, O.C.G. Adan, In-depth
687 investigation of thermochemical performance in a heat battery: Cyclic analysis of
688 K2CO3, MgCl2 and Na2S, Applied Energy. (2018).
689 https://doi.org/10.1016/j.apenergy.2018.01.083.

690 [24] P.A.J. Donkers, L.C. Sögütoglu, H.P. Huinink, H.R. Fischer, O.C.G. Adan, A review
691 of salt hydrates for seasonal heat storage in domestic applications, Applied Energy.
692 199 (2017) 45–68. https://doi.org/10.1016/j.apenergy.2017.04.080.

693 [25] H. Kerskes, Thermochemical Energy Storage, in: Storing Energy, Elsevier, 2016: pp.
694 345–372. https://doi.org/10.1016/B978-0-12-803440-8.00017-8.

695 [26] F. Desai, J. Sunku Prasad, P. Muthukumar, M.M. Rahman, Thermochemical energy
696 storage system for cooling and process heating applications: A review, Energy
697 Conversion and Management. 229 (2021) 113617.
698 https://doi.org/10.1016/j.enconman.2020.113617.

699 [27] Y. Chen, Z. Deng, Hydrodynamics of a droplet passing through a microfluidic T-
700 junction, Journal of Fluid Mechanics. (2017). https://doi.org/10.1017/jfm.2017.181.

701 [28] C. Zhang, F. Yu, X. Li, Y. Chen, Gravity–capillary evaporation regimes in
702 microgrooves, AIChE Journal. (2019). https://doi.org/10.1002/aic.16484.

703 [29] M. Liu, L. Su, J. Li, S. Chen, Y. Liu, J. Li, B. Li, Y. Chen, Z. Zhang, Investigation of
704 spherical and concentric mechanism of compound droplets, Matter and Radiation at
705 Extremes. (2016). https://doi.org/10.1016/j.mre.2016.07.002.

706 [30] Y. Chen, C. Zhang, M. Shi, Y. Yang, Thermal and hydrodynamic characteristics of
707 constructal tree-shaped minichannel heat sink, AIChE Journal. (2010).
708 https://doi.org/10.1002/aic.12135.

709 [31] C. Zhang, Y. Chen, R. Wu, M. Shi, Flow boiling in constructal tree-shaped
710 minichannel network, International Journal of Heat and Mass Transfer. (2011).
711 https://doi.org/10.1016/j.ijheatmasstransfer.2010.09.051.

712 [32] X. Daguenet-Frick, J. Bonjour, R. Revellin, Constructal microchannel network for
713 flow boiling in a disc-shaped body, IEEE Transactions on Components and Packaging
714 Technologies. (2010). https://doi.org/10.1109/TCAPT.2009.2027427.

715 [33] R. Wu, Y.P. Chen, J.F. Wu, M.H. Shi, Flow boiling characteristics in constructal tree-
716 shaped minichannel, Kung Cheng Je Wu Li Hsueh Pao/Journal of Engineering
717 Thermophysics. (2010).

718 [34] A. Sciacovelli, F. Gagliardi, V. Verda, Maximization of performance of a PCM latent
719 heat storage system with innovative fins, Applied Energy. (2015).

720 https://doi.org/10.1016/j.apenergy.2014.07.015.

721 [35] C. Zhang, J. Li, Y. Chen, Improving the energy discharging performance of a latent
722 heat storage (LHS) unit using fractal-tree-shaped fins, Applied Energy. (2020).
723 https://doi.org/10.1016/j.apenergy.2019.114102.

724 [36] J. LI, Y. Huang, C. Zhang, X. Liu, Numerical study on the solidification performance
725 of a latent heat storage unit with Koch-fractal fin, Fractals. 27 (2019) 1950108.
726 https://doi.org/10.1142/S0218348X19501081.

727 [37] M. Sheikholeslami, S. Lohrasbi, D.D. Ganji, Numerical analysis of discharging
728 process acceleration in LHTESS by immersing innovative fin configuration using
729 finite element method, Applied Thermal Engineering. (2016).
730 https://doi.org/10.1016/j.applthermaleng.2016.06.158.

731 [38] M. Sheikholeslami, S. Lohrasbi, D.D. Ganji, Response surface method optimization of
732 innovative fin structure for expediting discharging process in latent heat thermal
733 energy storage system containing nano-enhanced phase change material, Journal of the
734 Taiwan Institute of Chemical Engineers. (2016).
735 https://doi.org/10.1016/j.jtice.2016.08.019.

736 [39] COMSOL, Comsol, COMSOL Multiphysics User's Guide. (2020).
737 http://www.comsol.com. (accessed June 13, 2020).

738 [40] R. Olives, S. Mauran, A highly conductive porous medium for solid-gas reactions:
739 Effect of the dispersed phase on the thermal tortuosity, Transport in Porous Media. 43
740 (2001) 377–394. https://doi.org/10.1023/A:1010780623891.

741 [41] S.S. Ahamed, Kinetic investigation of K2CO3 using thermal analysis techniques and
742 modelling of Energy-PadsTM, 2018.

743 [42] K. Kant, A. Shukla, D.M.J. Smeulders, C.C.M. Rindt, Analysis and optimization of the
744 closed-adsorption heat storage bed performance, Journal of Energy Storage. 32 (2020)
745 101896. https://doi.org/10.1016/j.est.2020.101896.

746 [43] A.H. Shapiro, The dynamics and thermodynamics of compressible fluid flow, Vol. 1,

747 Ronald Press, New York, 1953.

748 [44] F. Duval, F. Fichot, M. Quintard, A local thermal non-equilibrium model for two-
749 phase flows with phase-change in porous media, International Journal of Heat and
750 Mass Transfer. 47 (2004) 613–639.
751 https://doi.org/10.1016/j.ijheatmasstransfer.2003.07.005.

752 [45] F.P. Incropera, D.P. DeWitt, T.L. Bergman, A.S. Lavine, F.P. Incropera, A.S. Lavine,
753 Fundamentals of Heat and Mass Transfer, John Wiley & Sons, 2011.

754 [46] S. Mitra, M. Muttakin, K. Thu, B.B. Saha, Study on the influence of adsorbent particle
755 size and heat exchanger aspect ratio on dynamic adsorption characteristics, Applied
756 Thermal Engineering. 133 (2018) 764–773.
757 https://doi.org/10.1016/J.APPLTHERMALENG.2018.01.015.

758 [47] H.B. Lu, N. Mazet, B. Spinner, Modelling of gas-solid reaction - Coupling of heat and
759 mass transfer with chemical reaction, Chemical Engineering Science. (1996).
760 https://doi.org/10.1016/0009-2509(96)00010-3.

761 [48] N. Mazet, M. Amouroux, B. Spinner, Analysis and experimental study of the
762 transformation of a non-isothermal solid/gas reacting medium, Chemical Engineering
763 Communications. 99 (1991) 155–174. https://doi.org/10.1080/00986449108911585.

764 [49] R.W. Pryor, P. Roger W. Pryor, Multiphysics modeling using COMSOL®: a first
765 principles approach, 1st ed., Jones & Bartlett Publishers, 2009.
766 http://www.comsol.com/support/books/mmuc/.

767